Hindawi Publishing Corporation
Journal of Nanotechnology
Volume 2013, Article ID 173625, 11 pages
http://dx.doi.org/10.1155/2013/173625

Research Article

The Effect of Vacuum Annealing of Magnetite and Zero-Valent Iron Nanoparticles on the Removal of Aqueous Uranium

R. A. Crane and T. B. Scott

Interface Analysis Centre, University of Bristol, 121 St. Michael's Hill, Bristol BS2 8BS, UK

Correspondence should be addressed to R. A. Crane; richardandrewcrane@gmail.com

Received 24 July 2013; Revised 22 August 2013; Accepted 4 September 2013

Academic Editor: Andrei Kolmakov

As-formed and vacuum annealed zero-valent iron nanoparticles (nano-Fe^0) and magnetite nanoparticles (nano-Fe_3O_4) were tested for the removal of uranium from carbonate-rich mine water. Nanoparticles were introduced to batch systems containing the mine water under oxygen conditions representative of near-surface waters, with a uranyl solution studied as a simple comparator system. Despite the vacuum annealed nano-Fe^0 having a 64.6% lower surface area than the standard nano-Fe^0, similar U removal (>98%) was recorded during the initial stages of reaction with the mine water. In contrast, ≤15% U removal was recorded for the mine water treated with both as-formed and vacuum annealed nano-Fe_3O_4. Over extended reaction periods (>1 week), appreciable U rerelease was recorded for the mine water solutions treated using nano-Fe^0, whilst the vacuum annealed material maintained U at <50 $\mu g\,L^{-1}$ until 4 weeks reaction. XPS analysis of reacted nanoparticulate solids confirmed the partial chemical reduction of U^{VI} to U^{IV} in both nano-Fe^0 water treatment systems, but with a greater amount of U^{IV} detected on the vacuum annealed particles. Results suggest that vacuum annealing can enhance the aqueous reactivity of nano-Fe^0 and, for waters of complex chemistry, can improve the longevity of aqueous U removal.

1. Introduction

Iron nanoparticles (hereafter nano-Fe^0) in recent years have received much attention as a potential alternative to conventional remediation technologies. By virtue of their size (0–100 nm) engineered nanoparticles offer a significantly greater surface area to volume ratio and higher surface energy [1] and resultantly offer similar or slightly enhanced reactivity to conventional materials but at a fraction of the mass. By using a smaller mass of reactive material to achieve the same objective (i.e., site remediation), both raw materials and energy are conserved [2], with significant potential savings in cost. The key driver behind the emergence of nano-Fe^0 for water treatment, however, is the advantage of subsurface deployment via injection as a liquid suspension, with the potential for aqueous contaminant treatment at almost any location and depth in terrestrial groundwater systems.

Although nano-Fe^0 have proven highly effective for the removal of a wide range of aqueous contaminants from simple synthetic solutions, in recent years, the performance of nano-Fe^0 for the remediation of chemically complex and/or "real" solutions in dissolved oxygen containing waters has yielded a contrasting result [3–7]. It has been outlined that the efficacy of nano-Fe^0 can be significantly lower in natural waters due to the presence of complexing agents that act to enhance the solubility of the metal and metalloid contaminant specie.

The mechanism of aqueous contaminant removal onto nano-Fe^0 is dependent on a wide range of factors including nanoparticle composition and physical structure, aqueous contaminant type, and groundwater chemistry. During oxidation, nano-Fe^0 are a source of $Fe^{II}_{(aq)}$, $Fe^{III}_{(aq)}$, H^+, H_2, and various precipitates such as $Fe(OH)_2$, $Fe(OH)_3$, Fe_3O_4, Fe_2O_3, FeOOH, and green rusts, with contaminant removal occurring in conjunction with the formation of such precipitate phases. In all cases, removal is driven by either sorption processes alone (adsorption, incorporation, complexation, etc.) or sorption followed by chemical reduction. Sorption of aqueous contaminant species onto nano-Fe^0 is possible

on either Fe^{II} or Fe^{III} surfaces; however, chemical reduction is only thermodynamically likely to occur on Fe^0 or Fe^{II} surfaces. It can therefore be stated that in order to maximise the aqueous chemical reduction potential of nano-Fe^0, maximum percentage mass of Fe^0/Fe^{II} must be preserved during storage prior to deployment. If this is not possible then an alternative method could be to chemically reduce nano-Fe^0 immediately prior to application. Another issue that has been documented to affect the aqueous reactivity of nano-Fe^0 synthesis is the presence of physical defects and chemical impurities [8, 9]. Thermal treatments, commonly used in metallurgy to refine grain structure, relieve internal stress, and produce equilibrium conditions, have been investigated in recent work as an appropriate method to refine the crystalline structure of nano-Fe^0 with simultaneous changes in surface chemistry [9, 10]. Particulates were annealed at 500°C for 24 hours and at a pressure of $<10^{-6}$ mbar, with the most noteworthy physiochemical changes including (i) the recrystallisation of the bulk metallic cores (leading to the diffusion bonding of some previously discrete nanoparticulates) and (ii) alterations to the nominally magnetite (Fe_3O_4) surface oxide (including thinning, dehydration, and migration of impurities toward surfaces and an increase in Fe^0/Fe^{2+} and Fe^{2+}/Fe^{3+} ratios). Magnetite has an inverse spinel structure that accommodates both Fe^{2+} and Fe^{3+} in octahedral sites and exhibits effective electron hopping between these sites. Consequently, magnetite is a strong semiconductor (10^2-$10^3\ \Omega^{-1}\ cm^{-1}$) and when formed as a film on metallic iron can facilitate electron transfer from the metal to the oxide, as previously reported [11]:

$$Fe^0 + 2Fe^{3+} \longrightarrow 3Fe^{2+} \quad E^0 = 1.21\ V. \tag{1}$$

Vacuum annealing of nano-Fe^0 has been observed to refine the stoichiometry of surface magnetite, even achieving substoichiometry ($Fe^{II}_{1+x}Fe^{III}_{2-x}O_4$) where oxygen vacancies are generated in order to compensate the negative charge introduced into the structure.

In a recent study by Crane et al. (2011) [3], nano-Fe^0 were tested for the removal of U from natural waters. The nanoparticles were observed as highly effective for the rapid removal of U despite any competing reactions with aqueous complexing agents, most notably carbonate. However, over extended time periods (>1 week)near-total rerelease of U was recorded. The current work presents a comparative study of as-formed and vacuum annealed nano-Fe^0 to determine how the changes imbued by vacuum annealing affect the aqueous reactivity and associated uranium removal efficacy of nano-Fe^0. In order to more closely assess the aforementioned interface reaction between bulk Fe^0 and surface oxide (predominantly Fe_3O_4) during nano-Fe^0 vacuum heat treatments, nanoscale magnetite (hereafter nano-Fe_3O_4) has also been adopted for use as a Fe^0-free comparator material.

2. Materials and Methods

2.1. Chemicals. All chemicals (iron (II,III) oxide nanopowder, iron sulphate ($FeSO_4 \cdot 7H_2O$), nitric acid (HNO_3), sodium borohydride ($NaBH_4$), sodium hydroxide (NaOH), uranyl acetate ($UO_2(CH_3COO)_2 \cdot 2H_2O$) and solvents (ethanol, acetone)) used in this study were of analytical grade and all solutions were prepared using Milli-Q purified water (resistivity > 18.2 MΩ cm).

2.2. The Uranium-Bearing Mine Water. The mine water used in the current study was taken from the Lişava uranium mine, Banat, Romania. The mine site is valley confined and bounded by limestone ridges which contribute significant concentrations of dissolved carbonate to ground and surface waters, a complexing agent that is recognised to significantly enhance U-mobility in environmental water systems [12]. The water is used for mining and is pumped from approximately 200 m below sea level, a depth significantly beneath the water table. It initially contains low concentrations of dissolved oxygen ($<3\ mg\ L^{-1}$); however, it quickly equilibrates with the atmosphere to reach oxygen concentrations more typical for that of vadose and/or surface waters ($\sim 10\ mg\ L^{-1}$), changing its redox potential and associated U^{VI} transport properties in the process.

2.3. Nanoparticle Synthesis. The pure Fe nanoparticles were synthesised using sodium borohydride to reduce ferrous iron to a metallic state, following an adaptation of the method described by Wang and Zhang (1997) [13]. 1.35 g of $FeCl_3 \cdot 6H_2O$ was dissolved in 50 mL of Milli-Q water, and then a 4 M NaOH solution was used to adjust the solution pH to 6.8. The addition of NaOH was performed slowly, dropwise, to avoid the formation of hydroxyl carbonyl complexes. The salts were reduced to metallic nanoparticles by the addition of 2.0 g of $NaBH_4$. The nanoparticle product was isolated through centrifugation (Hamilton Bell v6500 Vanguard centrifuge, 6500 RPM for 4 minutes), then sequentially washed with water, ethanol, and acetone (20 mL of each) and dried in a dessicator under low vacuum (approx. 10^{-2} mbar) for 48 hours. The nano-Fe_3O_4 was purchased from Sigma Aldrich (CAS number: 1317-61-9). Approximate 1 g quantities of nano-Fe^0 and nano-Fe_3O_4 were annealed in separate batches under vacuum ($<1 \times 10^{-6}$ mbar) at 500°C for 24 hours. Nanoparticles were stored in sealed containers within a nitrogen-filled Saffron Scientific glovebox until required.

2.4. Experimental Procedure. In order to maintain levels of DO similar to those measured in waters collected from culverts and settling ponds at the Lişava site ($7–13\ mg\ L^{-1}$), experiments involving as-formed and vacuum annealed nano-Fe^0 and nano-Fe_3O_4 were performed in sealed batch reactors in the open laboratory. A comparative uranyl solution at pH 8.5 was also studied as a single-system analogue. Five 500 mL Schott Duran jars were each filled with 400 mL of the U-contaminated mine water with three further jars filled with 400 mL of Milli-Q water with U at $0.5\ mg\ L^{-1}$, adjusted to pH 8.5 using 0.01 M NaOH. To one of the mine water solutions and one U^{VI} solution, 0.1 g of nano-Fe^0 suspended in 1 mL of ethanol (dispersed by sonication for 60 seconds

using a Fisher Scientific Ultrasonic cleaner) were added. The same was then performed for the vacuum annealed nano-Fe^0 (hereafter VA-nano-Fe^0). To two of the mine water solutions, as-formed and vacuum annealed nano-Fe_3O_4 were also added as comparator materials. The one remaining mine water solution and one remaining uranyl solution were also studied as nanoparticle-free control systems. Each system was sampled at 0 h, 1 h, 2 h, 4 h, 24 h, 48 h, 7 d, 14 d, 21 d, 28 d, and 84 d. Prior to sampling, the jars were gently agitated to ensure homogeneity, and pH, Eh and DO measurements were taken using a Hanna Instruments meter (model HI 8424) with a combination gel electrode pH probe, a platinum ORP electrode, and a Jenway 970 DO_2 meter, respectively. Aliquots of 10 mL were then taken from each jar and centrifuged at 6500 RPM using a Hamilton Bell Vanguard V6500 desktop centrifuge to separate the liquid and solid phases. The liquid was then decanted, filtered through a 0.22 μm cellulose acetate filter, and then prepared for solution analysis. The solid phase was prepared for analysis by sequential rinsing in 3 mL each of Milli-Q water, ethanol and then acetone, with the resultant suspension being pipetted onto an aluminium stub.

2.5. Sample Analysis Methods

2.5.1. BET. Prior to experiment, samples of each nanomaterial were analysed to determine surface area. In preparation for analysis, samples were degassed under, vacuum (1×10^{-2} mbar) for a 12-hour period at a temperature of 75°C. A known weight of the dried material was measured with a Quantachrome NOVA 1200 surface area analyser, using N_2 as the adsorbent and following a 7 point BET method.

2.5.2. ICP-AES Preparation and Conditions. The liquid samples were prepared for ICP-AES analysis by a 10-time dilution in 1% nitric acid (analytical quality concentrated HNO_3 in Milli-Q water). Blanks and standards for analysis were also prepared in 1% nitric acid, with Fe standards of 0.10, 0.25, 0.50, 1.00, 2.50, 5.0, and 10.0 mg L^{-1}. A Jobin Yvon Ultima ICP-AES (sequential spectrometer) fitted with a cyclone spray chamber and a Burgener Teflon Mira mist nebulizer was used. The Feconcentration was measured using the emission line at 259.94 nm.

2.5.3. ICP-MS Preparation and Conditions. Samples from each batch system were prepared for ICP-MS analysis by a 20-time dilution in 1% nitric acid (analytical quality concentrated HNO_3 in Milli-Q water). Blanks and U standards at 1.0, 2.0, 10, 20, and 50 μg L^{-1} were also prepared in 1% nitric acid. An internal Bi standard of 10 μg L^{-1} was added to blanks, standards, and samples. The ICP-MS instrument used was a Thermo Elemental Plasma Quad 3.

2.5.4. Transmission Electron Microscopy. TEM images were obtained with a JEOL JEM 1200 EX Mk 2 TEM, operating at 120 keV. Nanoparticle samples were mounted on 200 mesh holey carbon coated copper grids.

2.5.5. X-Ray Diffraction. A Phillips Xpert Pro diffractometer with a $Cu_{K\alpha}$ radiation source ($\lambda = 1.5406$ Å) was used for XRD analysis (generator voltage of 40 keV; tube current of 30 mA). XRD spectra were acquired between 2θ angles of 0–90°, with a step size of 0.02° and a 2 s dwell time.

2.5.6. X-Ray Photoelectron Spectroscopy. A Thermo Fisher Scientific Escascope equipped with a dual anode X-ray source ($Al_{K\alpha}$ 1486.6 eV and $Mg_{K\alpha}$ 1253.6 eV) was used for XPS analysis. Samples were analysed at $<5 \times 10^{-8}$ mbar with $Al_{K\alpha}$ radiation of 300 W (15 kV, 20 mA) power. High resolution scans were acquired using a 30 eV pass energy and 300 ms dwell times. Following the acquisition of survey spectra over a wide binding energy range, the Fe 2p, C 1s, O 1s and U 4f spectral regions were then scanned at a higher energy resolution such that valence state determinations could be made for each element. Data analysis was carried out using Pisces software [14], with binding energy values of the recorded lines being referenced to the adventitious hydrocarbon C1s peak at 284.8 eV. In order to determine the relative proportions of Fe^{2+} and Fe^{3+} in the sample analysis volume, curve fitting of the recorded Fe 2p photoelectron peaks was performed following the method of Grosvenor et al. (2004) [15]. The Fe 2p profile was fitted using photoelectron peaks at 706.7, 709.1, 710.6, and 713.4 eV corresponding to Fe^0, $Fe^{2+}{}_{\text{octahedral}}$, $Fe^{3+}{}_{\text{octahedral}}$, and $Fe^{3+}{}_{\text{terahedral}}$. These parameters were selected on the basis that the surface oxide was assumed to be a mixture of wüstite and magnetite, as the oxide Fe^{2+} is in the same coordination with the surrounding oxygen atoms in both forms of oxide.

3. Results and Discussion

3.1. Characterisation of the Unreacted Nanoparticles. TEM imaging recorded both nano-Fe^0 and nano-Fe_3O_4 as roughly spherical and loosely aggregated into chains (when dry), a feature attributed to magnetic and van der Waals attraction between adjacent particulates, Figure 1 [16]. Following vacuum annealing, the nanoparticulates were observed still to be arranged in chains and rings, but with some diffusion bonding between previously discrete points of contact (Figure 1). This was observed to have occurred most significantly for nano-Fe^0, evidenced by a large reduction in surface area (14.8 $\rightarrow$ 5.24 m^2 g^{-1} and 54.5 $\rightarrow$ 42.5 m^2 g^{-1} for nano-Fe^0 and nano-Fe_3O_4, resp.) determined by BET analysis, Table 1.

XRD data indicated that following annealing nano-Fe^0 recrystallised from particles of poorly crystalline/amorphous Fe^0 to α-Fe^0 with some constituent minor Fe_2B phases (Figure 2). However, no appreciable change was recorded for nano-Fe_3O_4 (Figure 3).

Concurrent XPS analysis of recorded Fe 2p photoelectron peaks confirmed the predominance of a mixed-valent iron oxide of near-stoichiometric magnetite for both as-formed nanoparticle types. Metallic iron was also recorded in the surface analysis volume, for the nano-Fe^0, indicating the oxide coating to be on the order of 3–5 nm thickness (corroborated by TEM analysis) see Table 1 and Figure 1.

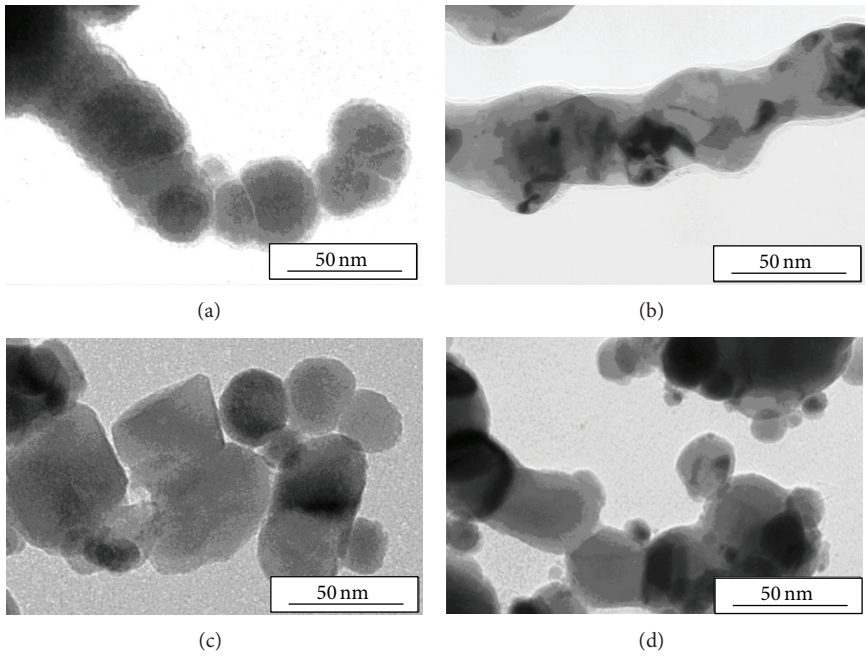

Figure 1: Transmission electron microscopy (TEM) images of nano-Fe^0 (a), VA-nano-Fe^0 (c), nano-Fe_3O_4 (b), and VA-nano-Fe_3O_4 (d).

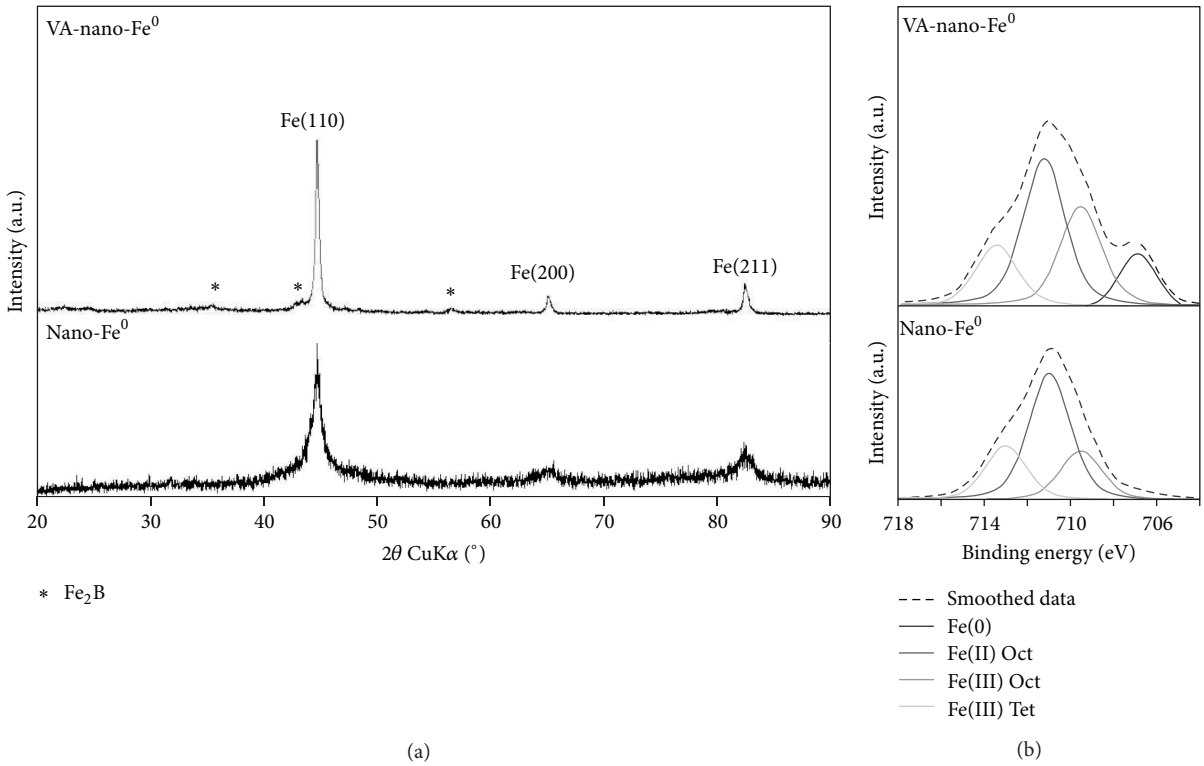

Figure 2: (a) X-ray diffraction (XRD) spectra acquired for nano-Fe^0 and VA-nano-Fe^0 for the range 20–90° 2θ. (b) X-ray photoelectron spectroscopy (XPS) Fe $2p_{3/2}$ photoelectron peaks for nano-Fe^0 and VA-nano-Fe^0.

Table 1: Bulk and surface properties of the nanomaterials.

Parameter	Analytical technique		Nano-Fe^0	VA-nano-Fe^0	Nano-Fe_3O_4	VA-Nano-Fe_3O_4
Particle size distribution (%)	XPS	0–60 nm	85	84	98	96
		60–100 nm	8	7	2	4
		>100 nm	7	9	0	0
Crystallinity	XRD		Highly disordered/amorphous (α-Fe)	Crystalline (α-Fe, Fe_2B)	Crystalline (Fe_3O_4)	Crystalline (Fe_3O_4)
Oxide thickness (nm)	TEM		3-4	2	—	—
Surface area ($m^2\ g^{-1}$)	BET		14.77	5.24	54.47	42.45
Surface composition (%)	XPS	Fe	40.5	22.5	21.51	26.78
		O	32.1	32.4	47.62	50.08
		C	14.5	19.1	30.81	23.14
		B	12.9	26.1	—	
Surface chemistry	XPS	$(Fe^0/Fe^{2+} + Fe^{3+})$	0.03	0.135	—	—
		Fe^{2+}/Fe^{3+}	0.33	0.45	0.31	0.30

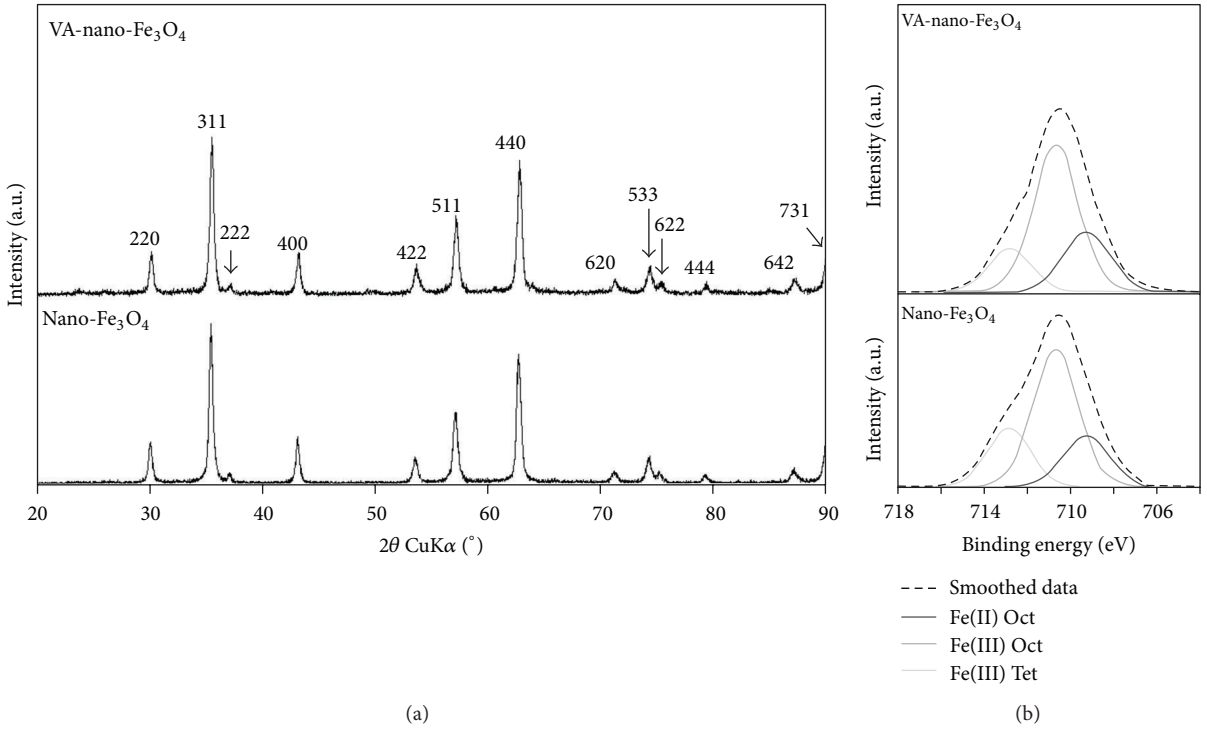

Figure 3: (a) X-ray diffraction (XRD) spectra acquired for nano-Fe3O4 and VA-Fe3O4 for the range 20–90° 2θ. (b) X-ray photoelectron spectroscopy (XPS) Fe $2p_{3/2}$ photoelectron peaks for nano-Fe_3O_4 and VA-Fe_3O_4.

Analysis of the recorded O 1s photoelectron peaks for the nano-Fe^0 determined a significantly greater proportion of surface sorbed water, in comparison to the nano-Fe_3O_4, that was subsequently removed as a result of vacuum annealing. The nano-Fe_3O_4 was also determined to be free of surface impurities, whilst the as-formed nano-Fe^0 were observed to have minor (<1 at. %) surface amounts of Na and more considerable amounts of C and B (≤14.5 at. %) as surface impurities. As a result of vacuum annealing, changes in Fe^{II}/Fe^{III} and Fe^0/Fe^{II} ratios were recorded for nano-Fe^0, from 0.33 → 0.45 and 0.03 → 0.14, respectively. In contrast, minimal change was recorded for VA-nano-Fe_3O_4. This was not unexpected considering only a single phase (magnetite) was present in the particulate, with no detectable amorphous

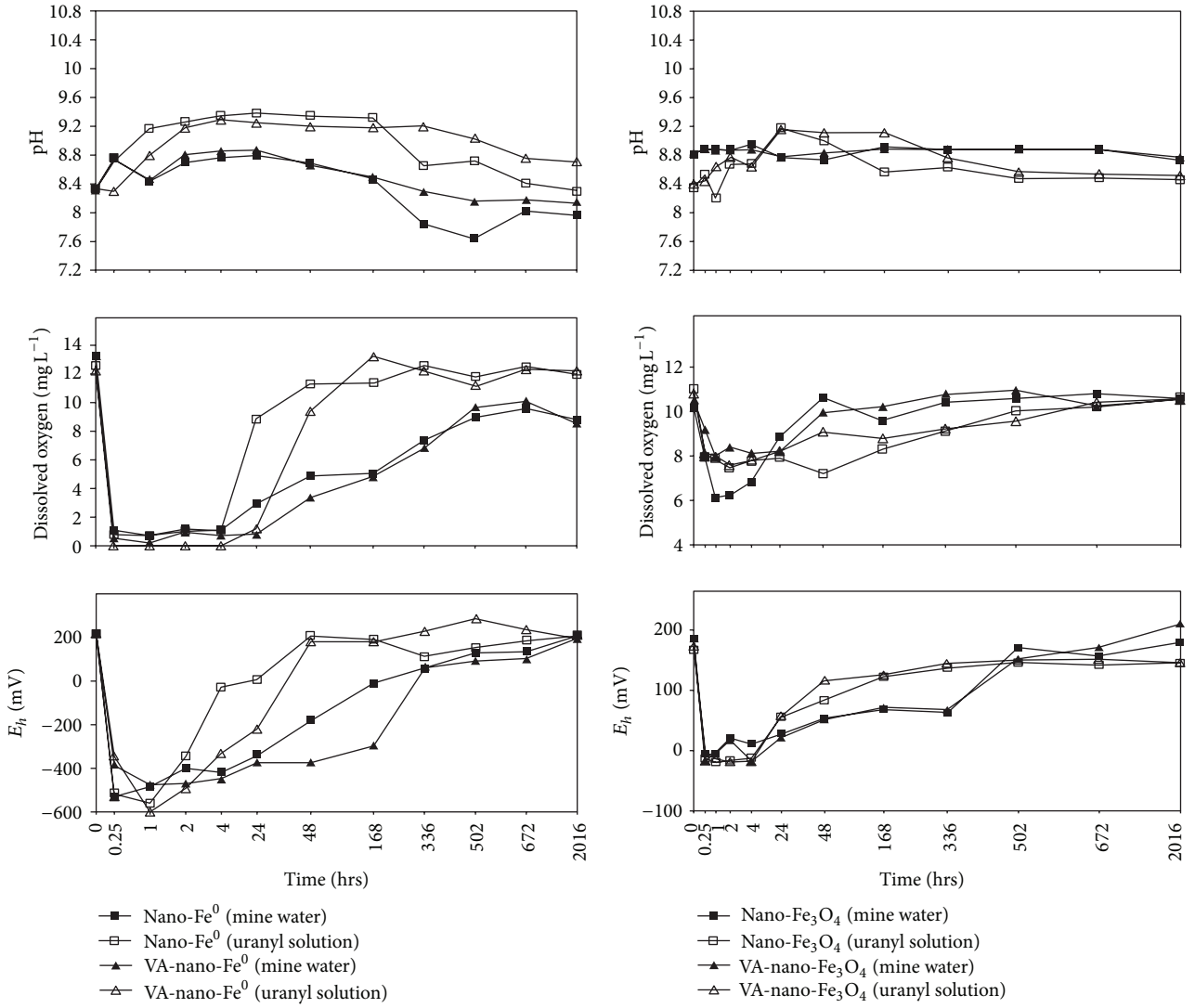

Figure 4: Solution pH, dissolved oxygen and Eh as a function of reaction time (0–2016 hrs).

component, and the heating temperature was below the wustite eutectic transformation point (570°C). A greater mass of surface impurity was also detected for the annealed nano-Fe^0, recording B and C contents of up to 26.1 at. % in the surface analysis volume, consistent with the formation of some minor carbide and boride phases.

3.2. Preliminary Characterisation of the Mine Water. Prior to nanoparticle addition, the mine water was characterised using ICP-AES and ICP-MS, with supplementary Eh, pH, and DO measurements, Table 2. HCO_3^-, well documented to increase the stability of dissolved U [12], was present at ~1000 mg L^{-1}.

3.3. Changes in DO/Eh/pH. For all experimental systems, the addition of nanoscale iron to the water samples resulted in a rapid shift to reducing conditions concurrent with a significant DO decrease and an increase in system pH (Figure 4). This is attributed to the rapid oxidation of nanoparticulate surfaces, consuming DO and H^+ and increasing the reduction potential of the system. The greatest system change was recorded during the first hour of reaction, with solutions treated with as-formed and vacuum annealed nano-Fe^0 exhibiting near-total DO consumption. Within this, most significant change was recorded for the uranyl solution, which is attributed to the lack of chemical buffers in comparison with the mine water.

Changes in pH/Eh/DO recorded for the vacuum annealed nano-Fe^0 systems were less than for the as-formed nano-Fe^0 systems. This is ascribed to the difference in relative surface areas between the two particulates. However, if we normalise the Eh change (from starting conditions of ~220 mV) to surface area, the VA-nano-Fe^0 show significantly greater manipulation of redox potential. For

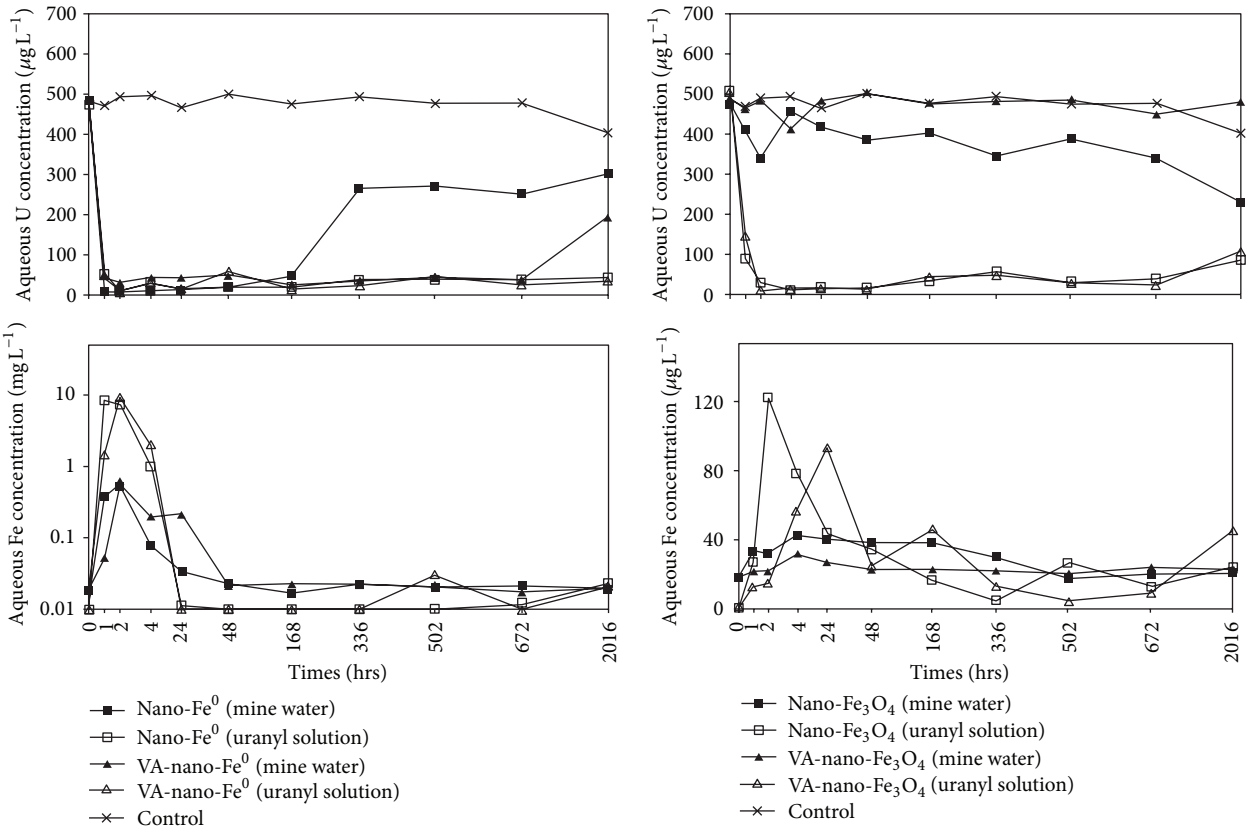

Figure 5: Aqueous uranium and iron concentrations as a function of reaction time (0–2016 hrs). The control is taken from the mine water system; a variation of <10 $\mu g\,L^{-1}$ was recorded in all other systems.

nano-Fe^0 and VA-nano-Fe^0, respectively, values of −50.8 and −114.8 mV m^{-2} were recorded for the mine water and −54.2 and −148.8 mV m^{-2} for a uranyl solution. Conversely, values of only −4.4 and −4.7 mV m^{-2} were recorded for nano-Fe_3O_4 and VA-nano-Fe_3O_4, with minimal concurrent pH/DO changes recorded. For all nano-Fe^0 systems, after 1 hour, near-total DO removal was recorded concurrent with further decreases in system Eh (to <−300 mV). These conditions were maintained up to 4 hours of reaction. Following this stage, a gradual recovery in system DO/Eh/pH was recorded in all systems and was observed to occur most rapidly for mine water solutions treated with the as-formed and vacuum annealed nano-Fe_3O_4, where most limited chemical reaction had occurred. For solutions treated using as-formed and vacuum annealed nano-Fe^0, the swiftest recovery in DO/Eh/pH was recorded for the uranyl solution and is attributed to a lack of chemical buffers in comparison with the more complex mine water solutions. All oxic reaction systems exhibited continued but limited pH increase to maxima after 24 hours, with a gradual decrease in pH over the remainder of the reaction period (to 84 days) ascribed to the formation of carbonic acid from atmospheric CO_2 ingress as previously suggested [3]. All systems after the 24 hour reaction recorded a gradual recovery in DO/Eh levels. This occurred most rapidly and comprehensively for the uranyl solution treated using both as-formed and vacuum annealed nano-Fe^0, which is attributed to the lack of chemical buffer species in comparison to the mine water.

3.4. Changes in Aqueous U Concentration. ICP-MS results indicated a rapid and near-total removal of U in all systems treated using as-formed and vacuum annealed nano-Fe^0 (Figure 5), with ≥95% removal in all systems within 2 hours of reaction, achieving concentrations of <30 $\mu g\,L^{-1}$, the limit specified for drinking water by the EPA (2011). This level of removal was maintained up to 48 hours of reaction time. Alternatively for both as-formed and vacuum annealed nano-Fe_3O_4, very little U removal was recorded over the entire duration of the experiment, with maximum removal (relative to the control) of ≤17%. Onwards, from 48 hours, a gradual increase in $U_{(aq)}$ concentration was recorded for the mine water solutions treated using nano-Fe^0 and ascribed to the oxidative dissolution of U previously removed on nanoparticle surfaces, with near total recovery in both systems recorded after 84-day reaction. In contrast, the VA-nano-Fe^0 exhibited extended retention of U with <50 $\mu g\,L^{-1}$ recorded until the end of the 4-week reaction period.

It is significant to note that the uranyl solution systems that were treated with as-formed and vacuum annealed nano-Fe^0 exhibited extended U retention (at ≥90%) for the duration of the experiment (84 days). Compared to the poor U

Table 2: Concentrations of notable chemical species present in the mine water, analysed by ICP-MS (U), ICP-AES (Fe, Mg, Cu, and Mo), volumetric titration (HCO_3^-, NO^{3-}, and PO_4^{3-}), gravimetry (SO_4^{2-}), and solvent extraction (organics) along with the recorded Eh, pH, and DO prior to nanoparticle addition.

Chemical species	Concentration (mg L^{-1})
Metals	
Cu	0.023
Fe	0.018
Mg	15.02
Mo	0.045
U	0.484
Ligands	
HCO_3^-	1041.10
NO_3^-	30.80
PO_4^{3-}	0.35
SO_4^{2-}	0.25
Organics	12.72
Solution conditions	
DO (mg L^{-1})	13.4
Eh (mV)	215
pH	8.36

retention exhibited in the mine water, systems this behaviour is ascribed to the lack of competitive chemical reactions as previously observed [3].

3.5. Changes in Aqueous Fe Concentration. With the additional use of ICP-AES, $Fe_{(aq)}$ concentrations were determined periodically in each batch system (Figure 5). $Fe_{(aq)}$ concentrations prior to nanoparticulate addition were determined as 0.018 mg L^{-1} for the mine water and undetected (considered zero) in the uranyl solutions. Following nanoparticle addition, maximum $Fe_{(aq)}$ concentrations were recorded in all systems within the first 48 hours of reaction and attributed to the rapid oxidative dissolution of nanoparticulate surfaces. In all systems, significantly greater Fe dissolution was recorded for uranyl solutions compared to the mine water, which is attributed to the lower initial ion content of the former with a subsequent lower likelihood for nanoparticle surface passivation during aqueous corrosion.

Compared to the as-formed material, greater Fe dissolution was recorded for vacuum annealed nano-Fe^0 for both the mine water and the uranyl solution, with an increase in maximum $Fe_{(aq)}$ values recorded. This was not unexpected, considering that the vacuum annealed particulate exhibited significantly enhanced Eh/pH/DO manipulation and U removal. In contrast, Fe dissolution was recorded as less for vacuum annealed nano-Fe_3O_4. This was not unexpected, given the minimal changes in bulk structure and surface chemistry imbued by vacuum annealing and a concurrent decrease in surface area (by 22.1%).

3.6. Characterisation of the Reacted Nanoparticulate Solids

3.6.1. X-Ray Diffraction. X-ray diffraction (XRD) was used to determine the bulk crystallinity and composition of as-formed and vacuum annealed nano-Fe^0 and nano-Fe_3O_4 solids extracted from the mine water systems at periodic intervals during the experiment (Figures 6 and 7). For as-formed and vacuum annealed nano-Fe^0, a transition from Fe^0, with peaks centred at 44.6, 65.6 and 82.6° 2θ corresponding to Fe(110), Fe(200), and Fe(211), respectively, to amorphous 2-line ferrihydrite ($5Fe_2O_3 \cdot 9H_2O$), with the two broad peaks recorded (centred at approximately 30° and 65° 2θ) corresponding to lattice reflections of (110) and (300), respectively [17, 18] was recorded throughout the reaction period. Comparing the as-formed and vacuum annealed nano-Fe^0, the latter material was recorded to exhibit a slower exhaustion of the starting Fe^0 material, with the Fe^0(110) diffraction peak detected after 7 days of reaction, whilst 100% conversion to Fe^{2+}/Fe^{3+} aqueous corrosion product was recorded for the as-formed nano-Fe^0. In addition, a minor peak centred at approximately 35.8° 2θ was recorded in the latter stages of the reaction (≥1 week) for both as-formed and vacuum annealed nano-Fe^0, which is ascribed to magnetite (Fe_3O_4), with a lattice reflection of (311). This was not unexpected seeing as magnetite is known to readily form in near-neutral to alkaline solutions via either (i) direct precipitation of a mixed Fe^{2+}/Fe^{3+} solution; (ii) oxidation of a Fe^{2+} solution via green rust or $Fe(OH)_2$; or (iii) the interaction of Fe^{2+} with ferrihydrite [19–21]. A second minor peak centred at 11.8° 2θ was also recorded for both nanomaterials, which is ascribed to akaganéite (β-FeOOH), with a lattice reflection of (110) [22]. The presence of chloride ions (which are necessary for akaganéite formation) was likely to have been provided by the dissolution of $FeCl_2$, present in the nano-Fe^0 due to incomplete conversion of $FeCl_2$ to Fe^0 (via chemical reduction using sodium borohydride) during the nano-Fe^0 synthesis. In the latter stages of the reaction (>7 days), the akaganéite peak was recorded to shift by approximately −0.5° 2θ, suggesting an increase in the lattice parameter of the material. This was most likely caused by a cationic substitution of a larger ion, such as Ca^{2+} (0.212 nm compared to 0.166 nm), into the lattice structure.

In contrast to the aforementioned relatively fast rate of aqueous corrosion recorded for the as-formed and vacuum annealed nano-Fe^0 and nano-Fe_3O_4, minimal change in nanoparticle composition was recorded for both as-formed and vacuum annealed nano-Fe_3O_4 throughout the 84-day reaction period. In addition, no appreciable difference was detected for the as-formed and vacuum annealed material. This provides additional evidence that vacuum annealing imbued minimal change to the corrosion behaviour of nano-Fe_3O_4.

3.6.2. X-Ray Photoelectron Spectroscopy. X-ray photoelectron spectroscopy (XPS) was used to study the changes in surface chemistry of as-formed and vacuum annealed nano-Fe^0 and nano-Fe_3O_4 solids extracted from the mine water systems at periodic intervals during the experiment (Figure 8). Curve fitting of the Fe $2p_{3/2}$ photoelectron peaks recorded a decrease in the Fe^{II}/Fe^{III} ratio throughout the reaction period for all nanoparticle types, ascribed to aqueous oxidation. This occurred most rapidly during the initial stages of the reaction,

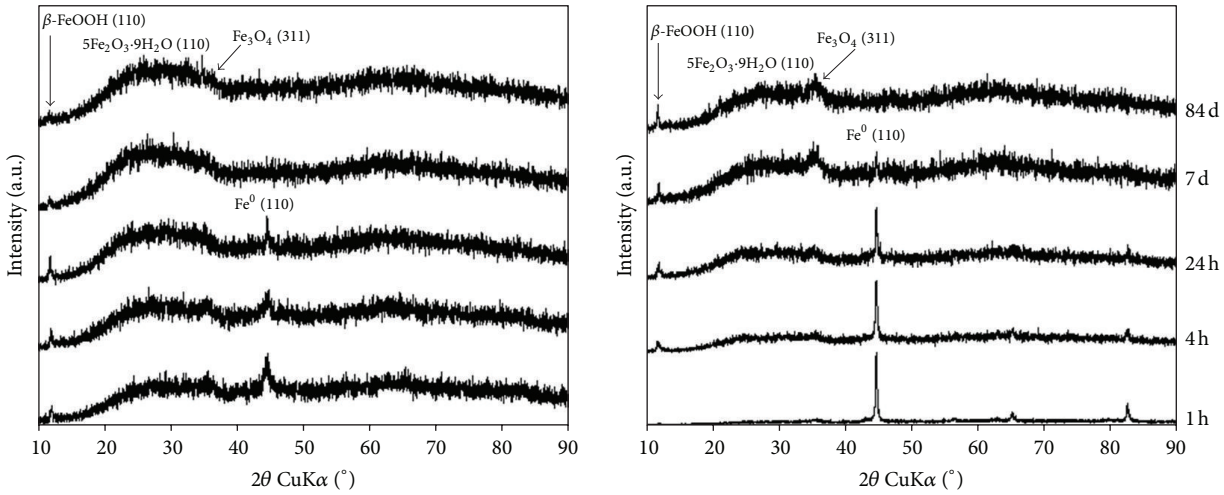

FIGURE 6: X-ray diffraction (XRD) spectra (for the range of 10–90° 2θ) recorded for the mine water batch systems containing as-formed (LHS) and vacuum annealed (RHS) nano-Fe^0 extracted at reaction times of 1 h, 4 h, 24 h, 7 d, and 84 d.

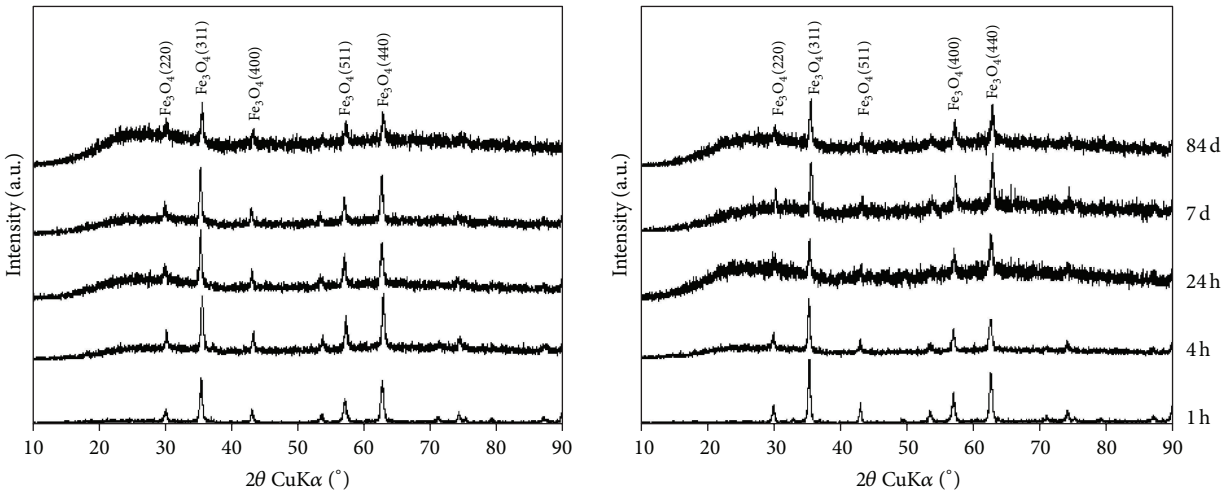

FIGURE 7: X-ray diffraction (XRD) spectra (for the range of 10–90° 2θ) recorded for the mine water batch systems containing as-formed (LHS) and vacuum annealed (RHS) nano-Fe_3O_4 extracted at reaction times of 1 h, 4 h, 24 h, 7 d, and 84 d.

with a shift in Fe^{II}/Fe^{III} ratios of 0.27 and 0.24 for nano-Fe^0 and VA-nano-Fe^0, respectively, and 0.29 and 0.28 for nano-Fe_3O_4 and VA-nano-Fe_3O_4 respectively. Following this initial and rapid oxidation phase, a gradual decrease in the Fe^{II}/Fe^{III} ratio was recorded with ratios after the 84-day reaction of 0.12 and 0.21 for as-formed and vacuum annealed nano- Fe^0, respectively, and 0.26 and 0.27 recorded for as-formed and vacuum annealed nano-Fe_3O_4 and VA-nano-Fe_3O_4, respectively.

XPS failed to record detectable peaks in the U 4f binding energy region of the recorded photoelectron spectra in all nanoparticle samples, with the exception of samples collected for as-formed and vacuum annealed nano-Fe^0 at 24 hours. This was not unexpected, given the small amount of U in each system (484 mg L^{-1}) relative to the large surface area presented by the nanoparticles (≥5.24 m^2). Subsequent curve fitting of the 24-hour data and following the method of Scott et al. (2005) [23] indicated that U present was in a partially reduced state for both systems with determined U^{IV}/U^{VI} ratios of 0.38 and 1.46, respectively, indicating that chemical reduction was more prevalent in the vacuum annealed nano-Fe^0 system.

4. Conclusions

Vacuum annealing at 500°C and 1×10^5 mbar for 24 hours has been shown in the current work to significantly improve the reactivity of nanoscale zero-valent iron particles. Results demonstrate that despite a decrease in surface area by 64.6% as a result of the vacuum annealing process, the vacuum annealed particles exhibited (i) similar U removal (≥95%) during the initial stages of reaction (≤24 hrs); (ii) improved U

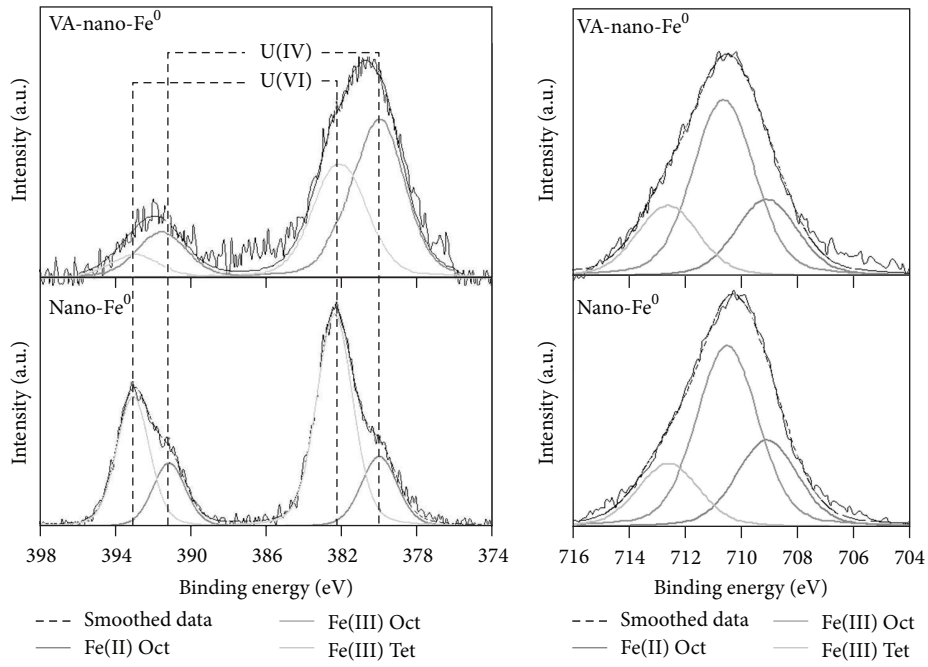

Figure 8: Curve fitted XPS U 4f (left) and Fe $2p_{3/2}$ (right) photoelectron peaks acquired after 24 hours reaction time for mine water solutions treated with as-formed and vacuum annealed nano-Fe^0.

retention over extended reaction periods (>1 week); and (iii) significantly enhanced redox (Eh) manipulation per unit surface area. The difference in reactivity is attributed to the formation of an effective electronic network within the annealed particles, related to (i) reordering and recrystallisation of the metallic cores; (ii) concurrent thinning, dehydration, and stoichiometric refinement (namely, an increase in Fe^{2+} relative to Fe^{3+}) of the surface oxide; and (iii) volatilisation and migration, of impurities toward the particle surfaces and grain boundaries. In comparison, minimal changes in the reactivity of the nanoscale magnetite particles were recorded as a result of the vacuum annealing process. This was not unexpected considering (i) only a single phase (magnetite) was present; (ii) the heating temperature (500°C) was below the wustite eutectic transformation point (570°C); and (iii) the material was determined using XRD and XPS as being highly crystalline and relatively free of impurity phases. It has therefore been demonstrated in the current work that the changes imbued by vacuum annealing are highly dependent upon (i) the composition and crystallinity of the starting material and (ii) the presence (or absence) of a metallic iron core.

Conflict of Interests

The authors declare that there is no conflict of interests regarding the publication of this paper.

Acknowledgments

The authors would like to thank Dr. Chung Choi (School of Earth Sciences) and Mr. Jonathan Jones (School of Chemistry) from the University of Bristol for performing ICP-AES and TEM analysis, respectively. This work was financially supported by NATO through the Cooperative Science and Technology Sub-Programme (CLG982551).

References

[1] W.-X. Zhang, "Nanoscale iron particles for environmental remediation: an overview," *Journal of Nanoparticle Research*, vol. 5, no. 3-4, pp. 323–332, 2003.

[2] T. Masciangioli and W.-X. Zhang, "Environmental technologies at the nanoscale," *Environmental Science and Technology*, vol. 37, no. 5, pp. 102A–108A, 2003.

[3] R. A. Crane, M. Dickinson, I. C. Popescu, and T. B. Scott, "Magnetite and zero-valent iron nanoparticles for the remediation of uranium contaminated environmental water," *Water Research*, vol. 45, no. 9, pp. 2931–2942, 2011.

[4] M. Dickinson and T. B. Scott, "The application of zero-valent iron nanoparticles for the remediation of a uranium-contaminated waste effluent," *Journal of Hazardous Materials*, vol. 178, no. 1–3, pp. 171–179, 2010.

[5] F. He, D. Zhao, and C. Paul, "Field assessment of carboxymethyl cellulose stabilized iron nanoparticles for in situ destruction of chlorinated solvents in source zones," *Water Research*, vol. 44, no. 7, pp. 2360–2370, 2010.

[6] S. Klimkova, M. Cernik, L. Lacinova, J. Filip, D. Jancik, and R. Zboril, "Zero-valent iron nanoparticles in treatment of acid mine water from in situ uranium leaching," *Chemosphere*, vol. 82, no. 8, pp. 1178–1184, 2011.

[7] T. B. Scott, I. C. Popescu, R. A. Crane, and C. Noubactep, "Nanoscale metallic iron for the treatment of solutions containing multiple inorganic contaminants," *Journal of Hazardous Materials*, vol. 186, no. 1, pp. 280–287, 2011.

[8] H. Cui, Y. Feng, W. Ren, T. Zeng, H. Lv, and Y. Pan, "Strategies of large scale synthesis of monodisperse nanoparticles," *Recent Patents on Nanotechnology*, vol. 3, no. 1, pp. 32–41, 2009.

[9] T. B. Scott, M. Dickinson, R. A. Crane, O. Riba, G. M. Hughes, and G. C. Allen, "The effects of vacuum annealing on the structure and surface chemistry of iron nanoparticles," *Journal of Nanoparticle Research*, vol. 12, no. 5, pp. 1765–1775, 2010.

[10] M. Dickinson, T. B. Scott, R. A. Crane, O. Riba, R. J. Barnes, and G. M. Hughes, "The effects of vacuum annealing on the structure and surface chemistry of iron:nickel alloy nanoparticles," *Journal of Nanoparticle Research*, vol. 12, no. 6, pp. 2081–2092, 2010.

[11] F. C. Camilo Moura, G. C. Oliveira, M. H. Araujo, J. D. Ardisson, W. A. De Almeida Macedo, and R. M. Lago, "Formation of highly reactive species at the interface Fe∘-iron oxides particles by mechanical alloying and thermal treatment: potential application in environmental remediation processes," *Chemistry Letters*, vol. 34, no. 8, pp. 1172–1173, 2005.

[12] K. V. Ragnarsdottir and L. Charlet, *Uranium Behaviour in Natural Environments, Environmental Mineralogy—Microbial Interactions, Anthropogenic Influences, Contaminated Land and Waste Management*, vol. 9 of *Mineralogical Society Series*, 2000.

[13] C.-B. Wang and W.-X. Zhang, "Synthesizing nanoscale iron particles for rapid and complete dechlorination of TCE and PCBs," *Environmental Science and Technology*, vol. 31, no. 7, pp. 2154–2156, 1997.

[14] "Dayta Systems Bristol UK," 2013, http://www.daytasystems.co.uk/.

[15] A. P. Grosvenor, B. A. Kobe, M. C. Biesinger, and N. S. McIntyre, "Investigation of multiplet splitting of Fe 2p XPS spectra and bonding in iron compounds," *Surface and Interface Analysis*, vol. 36, no. 12, pp. 1564–1574, 2004.

[16] L. Zhang and A. Manthiram, "Experimental study of ferromagnetic chains composed of nanosize Fe spheres," *Physical Review B*, vol. 54, no. 5, pp. 3462–3467, 1996.

[17] S. Das, M. J. Hendry, and J. Essilfie-Dughan, "Transformation of two-line ferrihydrite to goethite and hematite as a function of pH and temperature," *Environmental Science and Technology*, vol. 45, no. 1, pp. 268–275, 2011.

[18] L. E. Davidson, S. Shaw, and L. G. Benning, "The kinetics and mechanisms of schwertmannite transformation to goethite and hematite under alkaline conditions," *American Mineralogist*, vol. 93, no. 8-9, pp. 1326–1337, 2008.

[19] R. M. Cornell and U. Schwertmann, *The Iron Oxides: Structure, Properties, Reactions, Occurrences and Uses*, Wiley-VCH, 2003.

[20] T. Missana, M. García-Gutiérrez, and V. Fernńdez, "Uranium (VI) sorption on colloidal magnetite under anoxic environment: experimental study and surface complexation modelling," *Geochimica et Cosmochimica Acta*, vol. 67, no. 14, pp. 2543–2550, 2003.

[21] S. Mann, N. H. C. Sparks, S. B. Couling, M. C. Larcombe, and R. B. Frankel, "Crystallochemical characterization of magnetic spinels prepared from aqueous solution," *Journal of the Chemical Society, Faraday Transactions 1*, vol. 85, no. 9, pp. 3033–3044, 1989.

[22] E. Murad, "Mössbauer and X-ray data on β-FeOOH (akaganéite)," *Clay Minerology*, vol. 14, pp. 273–283, 1976.

[23] T. B. Scott, G. C. Allen, P. J. Heard, and M. G. Randell, "Reduction of U(VI) to U(IV) on the surface of magnetite," *Geochimica et Cosmochimica Acta*, vol. 69, no. 24, pp. 5639–5646, 2005.